textiles

MDPI

Article

Hybrid Taguchi–Composite Scoring Approach Framework for Multi-Objective Optimization of Ring Spinning Process: Yarn Tension, Cop Diameter and Yarn Breakage Rate

Emilija Toshikj [1,*] and Sijche Pechkova [2]

[1] Department of Textile Engineering, Faculty of Technology and Metallurgy, Ss. Cyril and Methodius University in Skopje, St. Rugjer Boskovic No. 16, 1000 Skopje, North Macedonia
[2] Department of Chemical and Control Engineering, Faculty of Technology and Metallurgy, Ss. Cyril and Methodius University in Skopje, St. Rugjer Boskovic No. 16, 1000 Skopje, North Macedonia; sijche@tmf.ukim.edu.mk
* Correspondence: tosic_emilija@tmf.ukim.edu.mk

Abstract

In this study, we investigate the optimization of ring spinning parameters affecting key yarn quality characteristics, including yarn tension, cop diameter, and end breakage. Experiments were conducted on cotton–polyester yarn using three process variables: traveler mass (60, 67.5, and 75 mg), spindle speed (12,900, 13,300, and 13,700 min^{-1}), and doff stage (43, 111, and 179 mm). A two-stage optimization method was applied: we used the Taguchi method to optimize individual responses, while a normalization-based composite scoring approach was used to integrate them to determine globally optimal ring spinning parameters under differing response-specific conditions. The results show that traveler mass is the dominant factor influencing yarn tension, contributing 65.48% and 73.29% of variation at the bottom and top ring rail positions, respectively. Cop diameter is primarily governed by doff stage, contributing 89.43% of total variance (ANOVA), with the intermediate level (111 mm) yielding the highest mean diameter and the most favorable S/N ratio. The yarn breakage rate is mainly affected by doff stage (57.26%) and spindle speed (41.89%), with minimum breakage observed at moderate spindle speed and mid-level doff stage. The global optimal parameter combination (60 mg traveler mass, 12,900 min^{-1} spindle speed, and 111 mm doff stage) achieved balanced multi-response performance. The framework demonstrates strong predictive capability ($R^2 > 0.991$) and enables optimization.

Keywords: ring spinning; multi-response optimization; yarn tension; cop diameter; end breakage; composite scoring

Received: 28 April 2026
Revised: 10 June 2026
Accepted: 18 June 2026
Published: 22 June 2026

1. Introduction

The textile manufacturing industry is undergoing rapid transformation driven by Industry 4.0, which integrates automation, cyber–physical systems, intelligent sensing, and data-driven analytics to enhance intelligent and connected production [1,2]. This evolution has increased the demand for high-performance, cost-efficient, and sustainable yarns, requiring continuous optimization of spinning processes that govern yarn structure and functionality during subsequent chemical treatments and finishing operations [3–5]. Several studies have emphasized the importance of yarn structural parameters in determining the efficiency of downstream textile processing and final product performance [6]. Moreover, the structural and mechanical properties established at the yarn stage directly influence

fabric appearance, durability, dimensional stability, and service life under repeated use and laundering conditions [7–9]. Consequently, improving yarn quality and spinning efficiency remains a major objective in modern textile manufacturing.

Among spinning technologies, ring spinning remains the dominant system for producing fine, compact, and mechanically strong yarns suitable for diverse textile applications [10]. Despite its industrial importance, the process involves complex interactions among mechanical, dynamic, and geometric phenomena. Process optimization and operational efficiency are therefore critical for achieving stable production performance [11]. Key parameters, including traveler mass, spindle speed, and ring rail movement, strongly influence yarn tension, balloon dynamics, winding behavior, package geometry, and yarn breakage [12–16]. Consequently, even small parameter variations can alter yarn path geometry and tension distribution, significantly affecting spinning stability and yarn quality.

Particularly important is the movement of the ring rail during cop formation. As the ring rail traverses between bottom and top positions, the geometry of the spinning system continuously changes, affecting balloon height, yarn path length, aerodynamic drag, and tension distribution [17]. These positional variations influence yarn deposition mechanisms, package density distribution, and cop geometry and therefore play a critical role in determining process stability and package formation quality. Nevertheless, positional effects associated with ring rail movement are frequently overlooked in optimization studies, which often rely on average response values and therefore may not fully capture the dynamic behavior occurring throughout the winding cycle.

Numerous studies have investigated the influence of spinning parameters on yarn quality and process performance. Analytical and experimental research has demonstrated that spindle speed, traveler mass, traveler–ring friction, balloon dynamics, winding geometry, and machine settings significantly affect yarn tension, spinning stability, cop morphology, package density, and yarn breakage behavior [18–20]. Although these studies have improved understanding of individual process mechanisms, most focus on isolated responses. Since yarn tension, cop formation, and yarn breakage are closely interconnected, single-response optimization may not adequately represent overall process performance or identify balanced operating conditions.

Various statistical optimization methods have been applied in spinning research, with the Taguchi method being particularly attractive due to its experimental efficiency and ability to identify robust parameter settings [21–23]. However, most studies remain focused on single-response optimization. Although multi-response techniques, including RSM, GRA, PCA, multivariate quality loss functions, and MANOVA-based approaches, have been reported [21,24,25], their application in ring spinning is limited. Moreover, optimum conditions are often determined from combined performance indices, making the relationships among individual response optima and associated trade-offs less explicit.

Several research gaps remain in ring spinning optimization. Integrated frameworks capable of simultaneously evaluating yarn tension, cop diameter, and yarn breakage are still limited, while positional effects associated with ring rail movement are often overlooked despite their influence on process stability. Furthermore, hybrid methodologies combining experimental design, predictive modeling, and multi-response optimization remain underutilized. Although regression-based models have recently been applied to predict textile properties and spectral responses [26], their integration with Taguchi-based optimization and positional response analysis remains scarce, limiting the systematic evaluation of conflicting performance responses and their underlying relationships.

Unlike conventional multi-response optimization approaches, including RSM, GRA, PCA-based optimization, and MANOVA-based ranking techniques [22,24,27], the proposed framework integrates response-specific Taguchi optimization, regression-based

prediction [26], positional response analysis, and a normalization-based composite scoring procedure. Previous studies have largely relied on combined performance indices while giving limited attention to ring-rail positional effects and the systematic evaluation of relationships and trade-offs among individual response optima [10,28,29].

In contrast, the present study first identifies response-specific optimum conditions for yarn tension, cop diameter, and yarn breakage at different ring rail positions. These individual optima are subsequently reconciled using a regression-assisted composite scoring procedure to determine a balanced global optimum. The framework enables interpretation of parameter effects, response prediction, and evaluation of trade-offs among competing performance characteristics while maintaining transparency through separate analysis of individual responses before their integration into an overall performance score.

Traveler mass, spindle speed, and doff stage were investigated using a Taguchi L9 experimental design, while both bottom and top ring rail positions were considered to capture positional variations during winding. Statistical analysis and regression modeling were applied to establish parameter–response relationships and support multi-response optimization. To the authors' knowledge, this integrated optimization framework has not previously been reported for ring spinning applications.

The proposed framework links yarn tension, cop formation, and yarn breakage within a unified optimization strategy. The results demonstrate that balanced control of traveler mass, spindle speed, and doff stage improves process stability, reduces yarn breakage, and maintains favorable cop geometry, providing a practical tool for multi-response optimization in ring spinning operations.

2. Materials and Methods

2.1. Materials

Yarns were produced from a fiber blend composed of Russian class I cotton and Maklen polyester fiber supplied by Hemtex (Skopje, North Macedonia). The blend composition contained 51% cotton and 49% polyester. The Russian I class cotton had a staple length of 33–34 mm, an effective fiber length of 32.5 mm, a mean fiber length of 16.0 mm, a linear density of 1.68 dtex, and a tensile strength of 4.4 cN/dtex. In contrast, the Maklen polyester fiber had a staple length of 38 mm, an effective length of 37.0 mm, a mean length of 37.3 mm, a linear density of 1.67 dtex, and a tensile strength of 7.6 cN/dtex. These fiber properties were selected to provide a balanced combination of natural and synthetic fiber characteristics suitable for ring spinning.

2.2. Yarn Spinning Procedure

A cotton carded yarn with a linear density of 20 tex and a twist level of 193 turns m^{-1} was produced using a TOYODA-type ring spinning frame (Toyota Industries Corporation, Kariya, Aichi, Japan) equipped with 465 spindles. The operating parameters of the spinning frame were spindle speeds of 12,900, 13,300, and 13,700 min^{-1}, traveler masses of 60, 67.5, and 75 mg; and doff stage heights of 43, 111, and 179 mm. The selected factor levels were chosen to represent low, intermediate, and high operating conditions within the practical processing range for the production of 20 tex cotton–polyester ring-spun yarn. These levels were selected to ensure stable machine operation while enabling sufficient variation to evaluate the effects of traveler mass, spindle speed, and doff stage on yarn tension, cop diameter, and yarn breakage rate. The chosen parameter ranges also enabled the identification of an optimal operating window within the investigated experimental domain.

2.3. Yarn Testing

2.3.1. Yarn Cop Diameter

The cop diameters at the bottom (cb) and top (ct) ring rail positions (base and apex of the cone, respectively) were measured on ring-spun cotton yarn cops under uniform winding conditions. Before testing, samples were conditioned at 21 ± 1 °C and 65 ± 2% relative humidity for at least 24 h in accordance with ASTM D1776/D1776M-20 to ensure moisture equilibrium. Measurements were taken at both the bottom and top ring rail positions to capture dimensional variation along the cop height. A digital Vernier caliper with ±0.01 mm accuracy was used. Each cop was positioned horizontally to avoid deformation, and the maximum transverse diameter was recorded. Five measurements at 120° intervals were taken for each cop and averaged. The procedure followed the specifications of ASTM D2258-01 (2020) with minor modifications for ring-spun cop geometry [30].

2.3.2. Yarn Tension

Yarn tension at the bottom (tb) and top (tt) ring rail positions (base and apex of the cone, respectively) was analytically estimated using a dynamic force-based model derived from traveler mechanics, consistent with the approach used in established ring spinning models [31]. This non-contact approach determined tension between the traveler and package using traveler mass, friction coefficient, ring radius, and spindle angular velocity. For each condition, five measurements were averaged. The analytical expression given in Equation (1) enables practical estimation of yarn tension in the traveler–package region during spinning, although it does not fully depict tension distribution along the spinning balloon. As the objective of this study was to evaluate the relative effects of process parameters under identical operating conditions rather than to characterize the full balloon behavior, this approximation was considered adequate for the investigated spindle speed range and machine configuration.

$$t = \frac{\mu \cdot m_t \cdot R^2 \cdot \omega^2}{r \cdot 10^3} \quad (1)$$

where t is the yarn tension between the traveler and the package (cN), and μ is the coefficient of friction between the traveler and the ring; the literature reports values typically ranging from 0.12 to 0.23 for ring–traveler systems operating at spindle speed between 10,000 and 14,000 min^{-1} [32,33], and in this study a constant value of μ = 0.12 was adopted for all calculations. Moreover, in Equation (1), m_t is the traveler mass (g), R is the radius of the ring (cm), ω is the spindle angular velocity (rad/s), and r is the radius of the package (cm).

This method offers several operational advantages, including its non-contact nature, low cost, minimal instrumentation requirements, and compatibility with in-process estimation without disrupting yarn flow.

2.3.3. Yarn Breakage Rate

The yarn breakage rate (e) was evaluated under industrial spinning conditions using the chronometric observation method [33]. During the observation period, all yarn breaks repaired by the operator were recorded together with the corresponding spindle numbers, while the number of operating spindles and the total observation time were documented for normalization. Five independent measurements were conducted for each condition and averaged. The breakage rate was expressed as the number of breaks per 1000 spindle·h and calculated using Equation (2). This formulation enables direct comparison of yarn stability across spinning conditions while accounting for both machine operation and production efficiency:

$$e = \frac{e_1 \cdot 1000}{Z \cdot t} \quad (2)$$

where e is the yarn breakage rate (breaks per 1000 spindle·h), e_1 is the total number of yarn breaks observed during the test period, Z is the number of spindles in operation on the machine, and t is the observation time (h).

2.4. Experimental Design

A two-stage optimization approach was applied to evaluate yarn quality under varying ring spinning conditions (Figure 1). In the first stage, the Taguchi method optimized individual responses, including cop diameter, yarn tension at the bottom and top ring rail positions, and the yarn breakage rate, identifying optimal factor levels. Since optimal conditions differed, a second stage was introduced to determine global parameters (Figure 1). A normalization-based composite scoring method integrated all responses into a single score, enabling the identification of the optimal parameter combination for balanced performance.

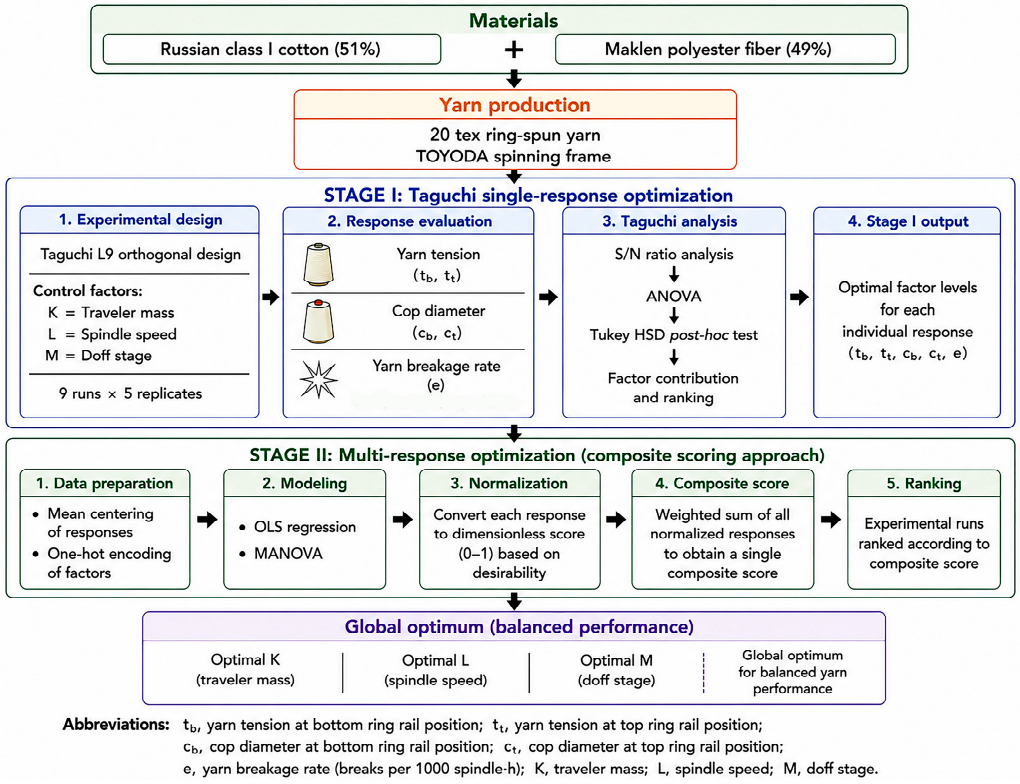

Figure 1. As schematic representation of the materials, experimental design, response evaluation, and two-stage optimization framework.

2.4.1. Taguchi-Based Experimental Design

In the first phase, the Taguchi method was applied to evaluate spinning parameters, enabling systematic multi-variable analysis while reducing experimental runs and improving efficiency without compromising statistical reliability (Figure 1) [34–36]. Three process parameters were selected as the control factors: traveler mass (K), spindle speed (L), and doff stage (M). Each factor was tested at three levels. Traveler masses were 60, 67.5, and 75 mg; spindle speeds were 12,900, 13,300, and 13,700 min^{-1}; and doff stage heights were 43, 111, and 179 mm. An L9 orthogonal array was used to design the experiments, enabling the efficient estimation of parameter effects with only nine experimental runs. For each experimental run, five replicate measurements were performed for each response variable and averaged to obtain a single representative response value. The resulting run means were used for the Taguchi and ANOVA analyses. Since the L9 orthogonal array consisted of nine experimental runs, the total degrees of freedom were calculated as $\text{df}_{\text{Total}} = 9 - 1 = 8$. Each factor was investigated at three levels and therefore contributed two degrees of free-

dom (3 − 1). Accordingly, K, L, and M each contributed df = 2, while the residual degrees of freedom were calculated as $df_{Residual} = 8 - (2 + 2 + 2) = 2$. Mean values and the grand mean were computed, and the responses were mean-centered to improve comparability, reduce bias, and standardize the dataset. Signal-to-noise (S/N) ratios were calculated using the Taguchi criteria [37], applying a larger-is-better approach (Equation (3)) for cop diameter and a smaller-is-better approach (Equation (4)) for yarn tension and breakage, followed by normalization relative to the overall mean for consistent comparison:

$$\eta_i = -10\log_{10}\left(\frac{1}{n}\sum_{j=1}^{n}\frac{1}{x_{ij}^2}\right) \quad (3)$$

$$\eta_i = -10\log_{10}\left(\frac{1}{n}\sum_{j=1}^{n}x_{ij}^2\right) \quad (4)$$

where η_i is the calculated performance measure (signal-to-noise ratio) in the ith run, n is the number of measurements in the run (number of trials), x_{ij} is the measure value in the jth trial and the ith experimental run, and x_{ij}^2 is the square of the measured value.

A one-hot encoded design matrix was used to represent categorical factors, followed by linear regression modeling. Factor significance was assessed using ANOVA ($p < 0.05$) with Tukey's HSD post hoc testing, and sum-of-squares decomposition quantified parameter contributions. Confirmation tests were conducted for five responses (tb, tt, cb, ct, e). Confidence intervals (95%) were calculated using ANOVA-derived parameters, including the F-ratio and the mean square error [25]. Agreement between predicted and experimental values within CI confirmed validity. Taguchi analysis was performed in Python 3 using the code provided in the Supplementary Materials (Python code phase I).

2.4.2. Composite Score Approach for Multi-Response Optimization

To reconcile conflicting optimal conditions obtained from Taguchi analysis, a second modeling phase employing a normalization-based composite scoring approach was implemented to evaluate the effects of factors K, L, and M on five responses: yarn tension at the bottom (tb) and top (tt) ring rail positions, cop diameter at the bottom (cb) and top (ct) positions, and end breakage (e) (Figure 1). This stage identifies globally optimal parameters when individual responses exhibit conflicting optima. Similar normalization-based aggregation strategies are commonly applied in the multi-response optimization of engineering systems [38]. Each factor was examined at three discrete levels, and all measured responses were mean-centered (Equation (5)) to remove the influence of absolute scale and highlight differences attributable to factor variation:

$$y'_{ij} = y_{ij} - \overline{y}_j \quad (5)$$

where y'_{ij} is the mean-centered value of the jth response variable for the ith experimental run, y_{ij} is the measured value, and $\overline{y}_j$ is the grand mean for that response.

To incorporate factors into the regression framework, dummy variables were generated using one-hot encoding. Each factor (K, L, M) at three levels (1, 2, 3) was represented by three binary indicator variables: K_{L1}, K_{L2}, and K_{L3}; L_{L1}, L_{L2}, and L_{L3}; M_{L1}, M_{L2}, and M_{L3}. For any given run, the indicator variable corresponding to the actual level was assigned a value of 1, while the remaining indicators for that factor were assigned 0. These dummy variables formed the predictor columns of the design matrix X, with a constant

term included for the intercept. The relationship between the predictors and each response was modeled using Ordinary Least Squares (OLS) regression using Equation (6):

$$y = X\beta + \epsilon \quad (6)$$

where y is the response vector, X is the design matrix containing dummy variables and intercept, β is the vector of regression coefficients, and ϵ is the residual error vector.

The OLS estimates were obtained using Equation (7).

$$\hat{\beta} = (X^{\intercal}X)^{-1}X^{\intercal}y \quad (7)$$

where $\hat{\beta}$ is the vector of estimated regression coefficients (including the intercept and slope terms), X is the design matrix containing the predictor variables (dummy variables from one-hot encoding and intercept term), $X^{\intercal}$ is the transpose of the design matrix X, and y is the vector of observed response values.

Separate models were fitted for normalized means and normalized signal-to-noise (S/N) ratios. To evaluate the combined influence of process parameters across all responses, multivariate analysis of variance (MANOVA) was applied (Equation (8)):

$$Y = XB + E \quad (8)$$

where Y is the response matrix, B is the coefficient matrix, and E is the residual matrix.

The fitted regression models were used to predict responses for the complete $3^3 = 27$ factorial combinations of K, L, and M. The predicted responses were normalized between 0 and 1 (Equation (9)):

$$x_{norm} = \frac{x - x_{min}}{x_{max} - x_{min}} \quad (9)$$

where x_{norm} is normalized predicted value, x_{min} is minimum predicted value for the response, and x_{max} is maximum predicted value for that response.

To facilitate multi-response optimization, a composite score was defined. For responses to be minimized (tb, tt, e) $s_{min} = 1 - x_{norm}$ was used. For responses to be maximized (cb, ct), $s_{max} = x_{norm}$ was used.

The overall composite score for each combination was calculated using Equation (10):

$$s_{score} = (1 - tb_{norm}) + (1 - tt_{norm}) + (1 - e_{norm}) + cb_{norm} + ct_{norm} \quad (10)$$

The configuration yielding the highest composite score was identified as the optimal combination of K, L, and M for achieving the most favorable morphological characteristics. Taguchi analysis was performed in Python 3 using code provided in the Supplementary Materials (Python code phase II).

3. Results and Discussion

3.1. Taguchi Optimization of Yarn Tension, Cop Diameter and the Yarn Breakage Rate Using Traveler Mass, Spindle Speed, and Doff Stage in Ring Spinning

3.1.1. Yarn Tension Response to Traveler Mass, Spindle Speed, and Doff Stage

Yarn tension values at the bottom and top ring rail positions are presented in Figure 2. At the bottom position, tension ranged from 36.6 cN (run 2) to 54.2 cN (run 6), with the lowest value recorded at K = 60 mg, L = 13,300 min^{-1}, and M = 111 mm and the highest value at K = 67.5 mg, L = 13,700 min^{-1}, and M = 43 mm. In contrast, consistently higher tensions were observed at the top position, ranging from 58.2 cN (run 1) to 88.2 cN (run 9), with the maximum tension recorded at K = 75 mg, L = 13,700 min^{-1}, and M = 111 mm. The higher tension at the top position was attributed to increased balloon height and longer

yarn length during upward ring rail movement, which enhanced air drag and dynamic loading [16,39]. During ring rail traverse, positional variation in yarn tension arises: at the apex, a smaller winding diameter and larger balloon geometry increase tension, whereas at the base, a larger diameter and shorter balloon reduce aerodynamic drag and improve mechanical leverage. Yarn tension also increased with traveler mass and spindle speed due to centrifugal and frictional forces [39,40].

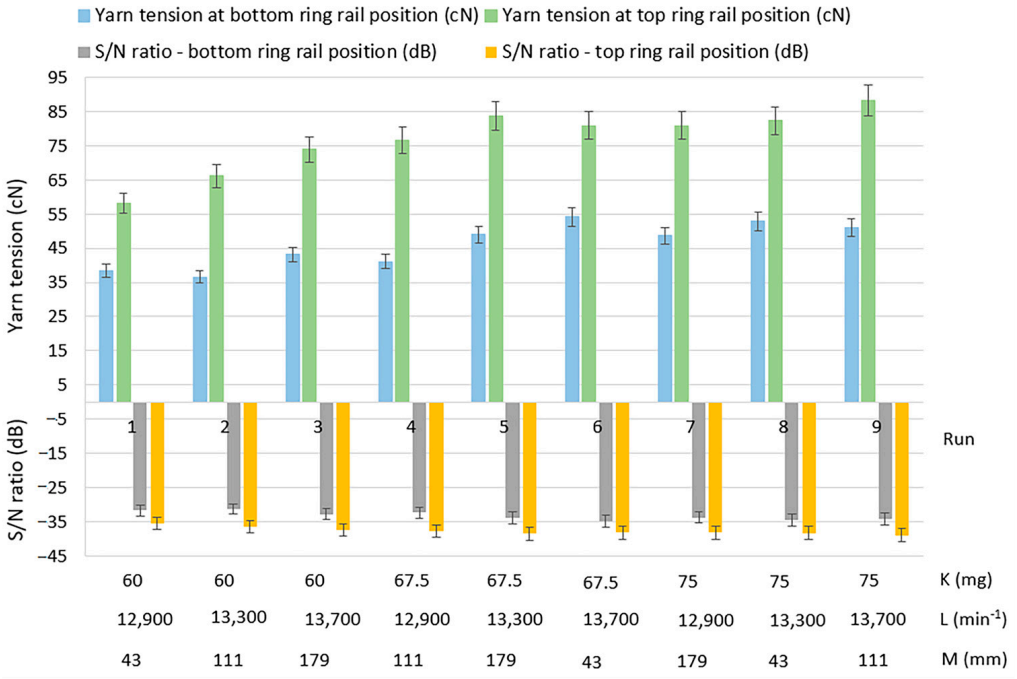

Figure 2. Yarn tension and corresponding signal-to-noise (S/N) ratios for the Taguchi L9 experimental runs at the bottom and top ring rail positions.

Signal-to-noise (S/N) ratios, based on the smaller-the-better criterion, further highlighted differences in variability. More negative S/N values were consistently observed at the top ring rail, indicating greater instability. The lowest S/N ratio (−38.909 dB) occurred in run 9, while the highest ratio (−31.270 dB) was recorded in run 2 at the bottom position, indicating the most stable condition. These trends aligned the with measured tension values, confirming that higher spindle speed and traveler mass reduced stability. Doff stage also influenced variability, with M2 (111 mm) improving stability at the bottom rail. The increased instability at the top was attributed to greater vertical displacement, balloon height, and increased yarn length within the balloon, which amplified air drag and inertial effects [16,39,40].

The S/N response table (Table 1) and main effect plots (Figure 3) illustrate the effects of the investigated factors (K, L, and M) on yarn tension at the bottom and top ring rail positions. At the bottom rail, traveler mass exhibited the strongest effect, with the S/N ratios decreasing from −31.882 dB (K1) to −34.107 dB (K3), followed by spindle speed (−32.565 to −33.835 dB), while the doff stage showed a non-linear response with optimal stability at M2 (−32.560 dB) (Table 1). Delta (Δ) values confirmed the ranking K (Δ = 2.225) > L (Δ = 1.269) > M (Δ = 1.046) (Table 1), with the optimal combination being K1L1M2 (Figure 3a). At the top rail, the S/N ratios decreased across all factor levels, with traveler mass again dominating (−36.355 to −38.452 dB) (Table 1). The optimal setting shifted to K1L1M1 (Figure 3b), and delta values similarly had the ranking K (Δ = 2.097) > L (Δ = 1.099) > M (Δ = 0.736).

Table 1. A response table for signal-to-noise ratios for yarn tension showing factor-level S/N, deltas, and ranks at the bottom and top ring rail positions.

Ring Rail Position	Level	K (mg)	L (min^{-1})	M (mm)
Bottom	1	−31.882 *	−32.565 *	−33.606
	2	−33.587	−33.175	−32.560 *
	3	−34.107	−33.835	−33.409
	Delta	2.225	1.269	1.046
	Rank	1	2	3
	Optimum	K1	L1	M2
Top	1	−36.355 *	−37.044 *	−37.252 *
	2	−38.099	−37.719	−37.666
	3	−38.452	−38.143	−37.988
	Delta	2.097	1.099	0.736
	Rank	1	2	3
	Optimum	K1	L1	M1

* Optimum parameter level.

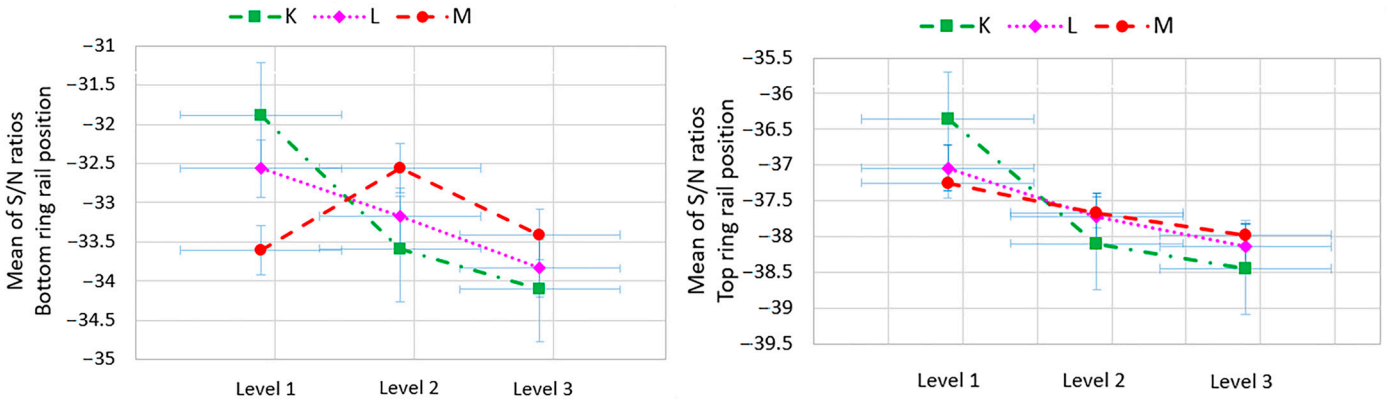

Figure 3. Main effect plots for signal-to-noise (S/N) ratios of yarn tension: (**a**) bottom ring rail position and (**b**) top ring rail position.

Traveler mass was the primary determinant of yarn tension. This is attributed to increased friction at the yarn–traveler interface, which results in higher mean tension [41,42]. Conversely, lower traveler mass reduced friction and improved stability, with K1 (60 mg) consistently yielding the least negative S/N ratios. Spindle speed was the second most influential factor; L1 (12,900 min^{-1}) reduced dynamic tension by limiting centrifugal forces and stabilizing balloon formation [43,44]. Doff stage had the least influence, with positional effects governing its behavior. The trends observed in Table 1 and Figure 3 were confirmed via ANOVA.

The ANOVA results for yarn tension (Table 2) quantify the statistical significance and ANOVA-derived contribution of each process parameter to total variance at the bottom and top ring rail positions. At the bottom rail, K was the dominant factor, accounting for 65.48% of the total variation ($F = 635.89$, $p = 0.00157$). L contributed 19.48% of the total variance ($p = 0.005258$), while M accounted for 14.93% of the total variance ($p = 0.006848$), indicating that all three parameters significantly influenced yarn tension at this position. At the top rail, traveler mass remained the most influential parameter, with a contribution of 73.29% of the total variance ($p = 0.012543$), followed by spindle speed at 17.86% of the total variance ($p = 0.049532$). In contrast, the doff stage had only a minor effect (7.92% of the total variance) and was statistically insignificant ($p = 0.105205$).

Table 2. ANOVA results for yarn tension at bottom and top ring rail positions, including factor contributions, F-value, and significance levels.

Ring Rail Position	Factors	df	Sum of Square (SS)	Mean Square (MS)	F	*p*	Contribution (%)
Bottom	K	2	8.126403	4.063202	635.888364	0.001570	65.481
	L	2	2.417767	1.208884	189.189479	0.005258	19.482
	M	2	1.853402	0.926701	145.028117	0.006848	14.934
	Residual	2	0.12780	0.006390			0.103
	Total	8	12.410352				100
Top	K	2	7.566527	3.783263	78.723999	0.012543	73.287
	L	2	1.844354	0.922177	19.189110	0.049532	17.864
	M	2	0.817478	0.408739	8.505246	0.105205	7.918
	Residual	2	0.096115	0.048057			0.931
	Total	8	10.324474				100

3.1.2. Cop Diameter Response to Traveler Mass, Spindle Speed, and Doff Stage

Figure 4 shows the effects of K, L, and M on cop diameter at the bottom and top ring rail positions. At the bottom position, the largest average diameter (42.3 mm) occurred in run 4 (K2L1M2), while the smallest (36.2 mm) was observed in run 6 (K2L3M1). In contrast, top positions had consistently smaller diameters (22.1–24.9 mm), indicating reduced yarn build-up efficiency at higher ring rail positions due to decreased deposition stability associated with a smaller winding diameter and increased balloon height during the traverse [39,40,45]. An inverse relationship between yarn tension and cop diameter was observed. Moderate tension levels promoted stable yarn guidance and efficient package build-up, resulting in the largest cop diameter, whereas excessive tension increased yarn compaction and restricted radial package growth. Consequently, the smallest cop diameter occurred under the highest tension conditions, suggesting reduced build-up efficiency and excessive package compression. Lower traveler mass (K1) contributed to reduced yarn tension and improved winding uniformity, thereby supporting effective package formation and larger cop diameters [45]. Top ring rail positions had smaller diameters due to cumulative tension effects during later doff stages. While M2 improved yarn layering, higher spindle speeds (L3) increased balloon instability through centrifugal forces, reducing winding uniformity. S/N ratio analysis (larger-the-better) further confirmed these trends. The bottom rail had higher S/N values (31.174–32.527 dB), indicating more stable and uniform cop diameter, whereas the top rail had lower S/N values (minimum 26.888 dB, run5), reflecting increased variability and reduced stability.

Table 3 and Figure 5 present the S/N response and main effect plots for cop diameter at three levels of K, L, and M at the bottom and top ring rail positions. At the bottom rail, the doff stage had the strongest influence, with the highest S/N ratio of 32.338 dB at M2 recorded for this factor, indicating improved diameter and reduced variability. Traveler mass and spindle speed exhibited minor variations, with S/N values of roughly 31.8 dB, confirming limited sensitivity. Delta (Δ) values ranked the factors as M (Δ = 1.022) > K (Δ = 0.260) > L (Δ = 0.249). The optimal combination for maximizing cop diameter was K1L1M2 (Table 3 and Figure 5a). This behavior is linked to yarn tension effects, where higher tension reduces cop diameter [46,47].

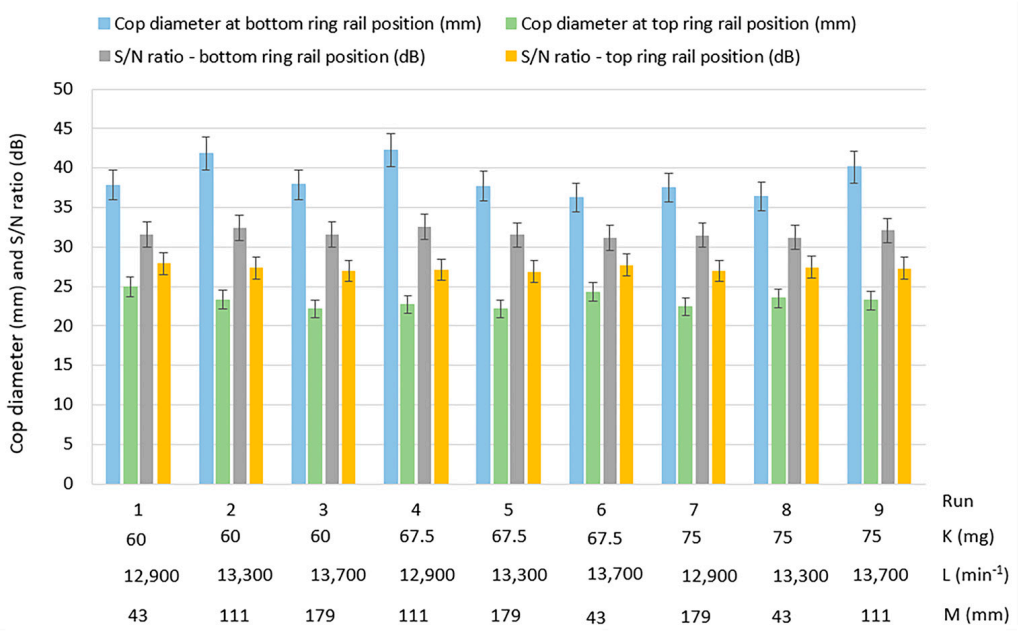

Figure 4. The cop diameters and corresponding signal-to-noise (S/N) ratios for the Taguchi L9 experimental runs at the bottom and top ring rail positions.

Table 3. A response table for the signal-to-noise ratios cop diameters showing factor-level S/N, deltas, and ranks at the bottom and top ring rail positions.

Ring Rail Position	Level	K (mg)	L (min^{-1})	M (mm)
Bottom	1	31.849 *	31.852 *	31.315
	2	31.743	31.724	32.338 *
	3	31.588	31.603	31.527
	Delta	0.260	0.249	1.022
	Rank	2	3	1
	Optimum	K1	L1	M2
Top	1	27.399 *	27.350 *	27.686 *
	2	27.240	27.219	27.259
	3	27.245	27.316	26.940
	Delta	0.159	0.131	0.746
	Rank	2	3	1
	Optimum	K1	L1	M1

* Optimum parameter level.

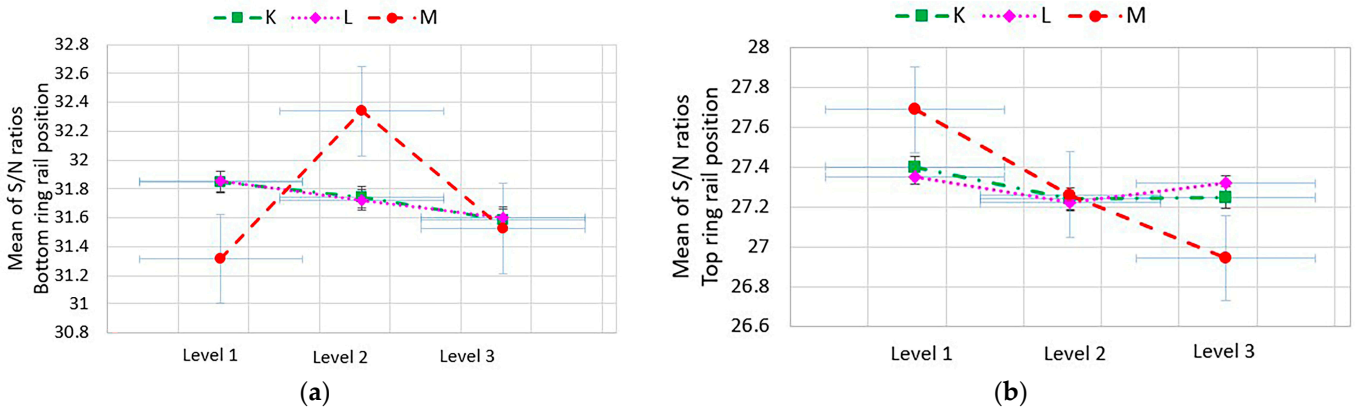

Figure 5. Main effect plots for the signal-to-noise (S/N) ratios of cop diameter: (**a**) bottom ring rail position and (**b**) top ring rail position.

At the top rail, parameter influence was weaker. The doff stage remained dominant, with the S/N ratios decreasing from 27.686 dB (M1) to 26.940 dB (M3), while traveler mass and spindle speed showed minimal effects. The optimal setting shifted to K1L1M1 (Figure 5b), with Δ values confirming a ranking of M (Δ = 0.746) > K (Δ = 0.159) > L (Δ = 0.131) (Table 3). Smaller cop diameters at the top were associated with increased yarn tension and reduced deposition stability. Cross-referencing with yarn tension showed that higher S/N ratios correspond to reduced tension and increased cop diameter, confirming their inverse relationship. Lower sensitivity at the top rail indicates reduced build-up efficiency during later doffing stages. Cop diameter is more influenced by positional factors related to ring rail movement than by mechanical parameters. The doff stage is a factor controlling cop diameter via deposition geometry [47–49]. These findings identify the doff stage as dominant for cop diameter via deposition geometry and layer formation, while traveler mass and spindle speed primarily affect tension, as confirmed via ANOVA.

The ANOVA results for cop diameter at the bottom and top ring rail positions (Table 4) show factor contributions and statistical significance. At the bottom rail, M was the dominant factor, accounting for 89.43% of total variation and representing the only statistically significant parameter (F = 163.67, p = 0.006073). K and L made minimal contributions (5.26% and 4.76%) and were not statistically significant. A similar trend was observed at the top rail, where the doff stage remained dominant (83.67%), although it was not statistically significant at the 95% level (F = 9.65, p = 0.093873).

Table 4. ANOVA results for cop diameter at the bottom and top ring rail positions, including factor contributions, F-value, and significance levels.

Ring Rail Position	Factors	df	Sum of Square (SS)	Mean Square (MS)	F	*p*	Contribution (%)
Bottom	K	2	0.102708	0.051354	9.618787	0.094173	5.256
	L	2	0.093104	0.046552	8.719382	0.102887	4.764
	M	2	1.747713	0.873856	163.67631	0.006073	89.434
	Residual	2	0.010678	0.005339			0.546
	Total	8	1.954203				100
Top	K	2	0.049110	0.024555	0.564158	0.63322	4.890
	L	2	0.027820	0.013958	0.319588	0.757812	2.770
	M	2	0.840257	0.420129	9.652650	0.093873	83.671
	Residual	2	0.087049	0.043525			8.668
	Total	8	1.004236				100

Contributions from traveler mass (4.89%) and spindle speed (2.77%) remained negligible. These findings contrast with the results for yarn tension (Table 2), where traveler mass was the dominant factor (65.48% at bottom, 73.29% at top), while the doff stage had a lesser influence. This divergence highlights a process trade-off: cop diameter is primarily governed via geometric deposition controlled by the doff stage, whereas yarn tension is driven by frictional and centrifugal forces associated with traveler mass. Therefore, effective process optimization requires a multi-objective approach to balance yarn tension stability and cop formation quality.

3.1.3. Yarn Breakage Rate Response to Traveler Mass, Spindle Speed, and Doff Stage

Values for the yarn breakage rate (Figure 6) ranged from 9 to 28 breaks per 1000 spindle·h, with the lowest value observed in run 4 and the highest in run 3. Yarn tension varied from 36.6 to 54.2 cN at the bottom rail ring and from 58.2 to 88.2 cN at the top ring rail (Figure 2), confirming the presence of consistently higher tension at the upper position. Cop diameter ranged between 36.2 and 42.3 mm at the bottom and between 22.1 and 24.9 mm at the top

(Figure 4), indicating clear positional dependence. Lower breakage values were generally associated with moderate tension levels and larger cop diameters, reflecting improved spinning stability under the selected parameter combinations. Run 4 showed optimal performance with low breakage, moderate tension, and large cop diameter, while run 3 indicated instability; S/N analysis confirmed that run 4 was the most stable condition overall. The variation in the yarn breakage rate is governed by the interplay between tension dynamics and deposition geometry. Lower breakage values correspond to stabilized balloon behavior and reduced tension fluctuations, which minimize cyclic stress and failure probability [40,50]. Increased tension at the top ring rail is attributed to increased balloon size and centrifugal forces, leading to greater instability and breakage propensity [51]. The larger cop diameters observed at the bottom position confirm the occurrence of more efficient yarn deposition and layer formation here [48–50]. These findings indicate that process stability is achieved through balanced tension control and optimized winding geometry, highlighting the coupled influence of mechanical and positional factors on yarn integrity.

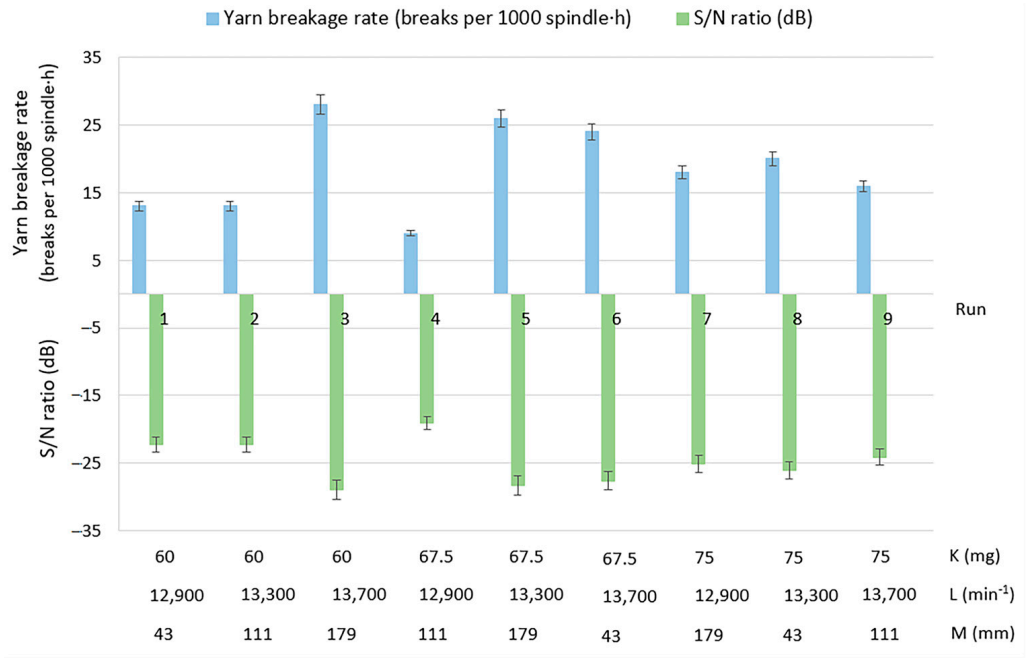

Figure 6. The yarn breakage rate and corresponding signal-to-noise (S/N) ratios for the Taguchi L9 experimental runs at the bottom and top ring rail positions.

Table 5 and Figure 7 present the S/N response and main effect plots for the yarn breakage rate, evaluating the effects of K, L, and M. The highest S/N ratio (−24.500 dB), indicating minimum breakage, was observed at K1 (60 mg). Delta (Δ) values established the influence hierarchy ranking as M (Δ = 5.643) > L (Δ = 4.720) > K (Δ = 0.569) (Table 5), identifying the optimal combination as K1L1M2 (Figure 7). These findings were consistent with yarn tension (Table 1) and cop diameter (Table 3), where the same parameter set produced favorable results at the bottom ring rail position. Specifically, K1 and L1 minimized variability in tension, while M2 (111 mm) improved cop geometry and reduced tension peaks. The S/N analysis confirmed the doff stage as the dominant factor controlling breakage, with the intermediate level (M2) optimizing yarn path stability and winding consistency. Lower spindle speeds reduced breakage by limiting dynamic ballooning effects [52]; in this study, L1 (12,900 min^{-1}) improved process stability. Although traveler mass had the smallest delta, it remained important for fine-tuning yarn tension behavior.

Table 5. A response table for the signal-to-noise ratios for the yarn breakage rate showing factor-level S/N ratios, deltas, and ranks at the bottom and top ring rail positions.

Level	K (mg)	L (min^{-1})	M (mm)
1	−24.500 *	−22.156 *	−25.301
2	−24.996	−25.533	−21.815 *
3	−25.070	−26.877	−27.449
Delta	0.569	4.720	5.643
Rank	3	2	1
Optimum	K1	L1	M2

* Optimum parameter level.

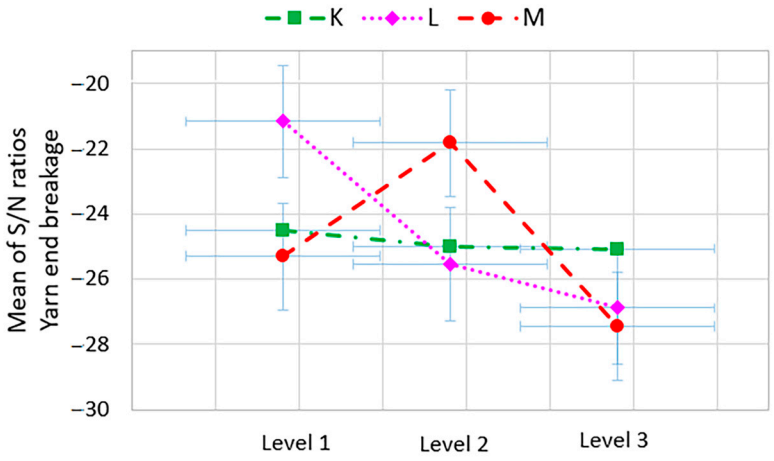

Figure 7. Main effect plots for the signal-to-noise (S/N) ratios of the yarn breakage rate.

Table 6 presents the ANOVA results for the yarn breakage rate, evaluating the effects of K, L, and M. The doff stage was the dominant factor, contributing 57.26% of the total variation (F = 319.71, p = 0.003118), followed by spindle speed at 41.89% (F = 233.89, p = 0.004257). Traveler mass made a negligible contribution (0.68%, F = 3.79, p = 0.20872). These results support the idea that the optimal parameter combination was K1L1M2 (Figure 6), where the intermediate doff stage (M2 = 111 mm) minimized breakage. The dominance of doff stage aligns with its strong influence on cop diameter (Table 4) and moderate effect on yarn tension (Table 2), highlighting its critical influence on spinning performance. The doff stage governs yarn layering and tension stability, influencing breakage behavior [52]. This was confirmed in this study, where the lowest breakage was obtained at the intermediate doff stage. Spindle speed also significantly affected breakage, as higher speeds increased balloon instability and tension fluctuations. In contrast, traveler mass had a limited direct effect on breakage, although it remains important for controlling yarn tension.

Table 6. ANOVA results for the yarn breakage rate including factor contributions, F-values, and significance levels.

Factors	df	Sum of Square (SS)	Mean Square (MS)	F	p	Contribution (%)
K	2	0.575207	0.287604	3.7911	0.208720	0.679
L	2	35.486437	17.743218	233.885478	0.004257	41.886
M	2	48.507610	24.253805	319.705966	0.003118	57.256
Residual	2	0.151726	0.075863			0.179
Total	8	84.72098				100

From a mechanistic perspective, the observed response behavior is governed by traveler–ring friction, balloon dynamics, yarn path geometry, and package formation during ring spinning [16,34,45,52]. Increasing traveler mass and spindle speed increases frictional, centrifugal, and aerodynamic forces, resulting in higher yarn tension and reduced balloon stability [16,34]. Higher ring rail positions further increase balloon height and unsupported yarn length, amplifying drag and tension fluctuations [45,52].

Yarn tension directly influences package formation. Excessive tension promotes yarn compaction, restricting radial package growth and reducing cop diameter, whereas moderate tension enables stable yarn deposition and efficient package build-up [46]. Simultaneously, the doff stage alters yarn path geometry, winding angle, and layer formation through changes in ring rail position, strongly affecting cop diameter and yarn breakage frequency. Consequently, traveler mass primarily governs yarn tension, while the doff stage exerts the strongest influence on cop formation and breakage behavior. These interacting mechanisms explain the differing optimum conditions observed for individual responses and demonstrate the need for multi-response optimization to achieve stable spinning performance, balanced package geometry, and reduced yarn breakage.

3.1.4. Validation of the Predicted Model for Yarn Tension, Cop Diameter, and Yarn Breakage Rate in Ring Spinning

The confirmation analysis in Table 7 validates the reliability and predictive capability of the hybrid framework integrating the Taguchi design and normalization-based composite scoring for key ring spinning responses, including yarn tension (tb, tt), cop diameter (cb, ct), and the yarn breakage rate (e). Predicted values showed close agreement with experimental results, with low percentage errors for yarn tension (3.02% for tb and 0.13% for tt) and cop diameter (0.24% for cb and 0.89% for ct), confirming high predictive accuracy. All predicted values fell within their respective confidence intervals, supporting the statistical robustness of the model. For the yarn breakage rate, the predicted value (6.889 breaks per 1000 spindle·h) slightly exceeded the experimental value (6 breaks per 1000 spindle·h), corresponding to a deviation of 14.81%. This deviation may also reflect the inherently discrete and stochastic nature of breakage events, influenced by fiber irregularities, transient tension fluctuations, and drafting instabilities [53]. Despite this, the prediction remained within the confidence interval, indicating satisfactory model performance.

Table 7. Confirmation results for experimental and predicted values of yarn tension and cop diameter at bottom and top ring rail position, and yarn breakage rate.

Response	Ev1 *	Ev2 *	Ev3 *	Ev4 *	Ev5 *	Evmean *	Predicted Value	CI Range	Error (%)
tb	33.1	34.5	33.9	33.7	33.8	33.8	32.778	30.146–35.410	3.02
tt	58.2	57.5	58.9	58.2	58.1	58.3	58.222	52.963–63.482	0.13
cb	42.8	43.8	42.0	42.7	43.1	42.4	42.500	41.167–43.833	0.24
ct	25.2	24.6	24.9	24.7	25.1	24.9	24.678	22.516–26.839	0.89
e	6	6	7	7	6	6.0	6.889	4.359–9.419	14.81

* Experimental values.

3.2. Composite Scoring Approach for Multi-Response Optimization in Ring Spinning

A normalization-based composite scoring approach was employed for multi-response optimization, where normalized responses were aggregated into a single dimensionless score to identify the optimal parameter combination. Equal weights were assigned to all responses to provide an unbiased assessment of overall process performance and to avoid introducing subjective assumptions regarding response importance. This approach was considered appropriate because the objective was to develop a general multi-response optimization framework rather than optimize the process for a specific industrial priority.

Nevertheless, the relative importance of yarn tension, cop diameter, and the yarn breakage rate may vary depending on production requirements. OLS regression models using K, L, and M were developed for five responses (tb, tt, cb, ct, and e). All models exhibited high coefficients of determination ($R^2 > 0.991$), indicating that a substantial proportion of the response variability was explained by the selected process parameters (Table 8). Nevertheless, because the regression models were developed from a Taguchi L9 orthogonal array comprising a limited number of experimental runs, the potential for model overfitting cannot be completely excluded, particularly when categorical factor levels are represented through dummy-variable encoding. To evaluate model robustness while accounting for predictor complexity, adjusted R^2 values were additionally calculated and they are reported in Table 8. For most responses, the adjusted R^2 values remained high (0.978–0.989), demonstrating that the explanatory power of the models was largely preserved after penalization for the number of predictors. Predicted values showed good agreement with the experimental observations for yarn tension, cop diameter, and the yarn breakage rate and remained within the corresponding confidence intervals, supporting model reliability even for the top cop diameter model (ct).

Table 8. Regression equations for ring spinning process responses.

Response	Regression Equation	R^2	Adj. R^2
tb	$y = -1.111 \cdot 10^{-5} - 6.7111 \cdot K_1 + 2.0222 \cdot K_2 + 4.6889 \cdot K_3 - 3.3778 \cdot L_1 + 0.0556 \cdot L_2 + 3.3222 \cdot L_3 + 2.3889 \cdot M_1 - 3.2111 \cdot M_2 + 0.8222 \cdot M_3$	0.997	0.988
tt	$y = 1.111 \cdot 10^{-5} - 10.6889 \cdot K_1 + 3.6778 \cdot K_2 + 7.0111 \cdot K_3 - 4.8556 \cdot L_1 + 0.6111 \cdot L_2 + 4.2444 \cdot L_3 - 2.9556 \cdot M_1 + 0.2444 \cdot M_2 + 2.7111 \cdot M_3$	0.995	0.978
cb	$y = -2.222 \cdot 10^{-5} + 0.5778 \cdot K_1 + 0.0778 \cdot K_2 - 0.6556 \cdot K_3 + 0.5444 \cdot L_1 + 0.0444 \cdot L_2 - 0.5889 \cdot L_3 - 1.8556 \cdot M_1 + 2.8111 \cdot M_2 - 0.9556 \cdot M_3$	0.995	0.980
ct	$y = -1.111 \cdot 10^{-5} + 0.2889 \cdot K_1 - 0.1444 \cdot K_2 - 0.1444 \cdot K_3 + 0.1556 \cdot L_1 - 0.2111 \cdot L_2 + 0.0566 \cdot L_3 + 1.0556 \cdot M_1 - 0.1111 \cdot M_2 - 0.9444 \cdot M_3$	0.991	0.664
e	$y = -2.222 \cdot 10^{-5} - 0.5556 \cdot K_1 + 1.1111 \cdot K_2 - 0.5556 \cdot K_3 - 5.2222 \cdot L_1 + 1.1111 \cdot L_2 + 4.1111 \cdot L_3 + 0.4444 \cdot M_1 - 5.8889 \cdot M_2 + 5.4444 \cdot M_3$	0.997	0.989

The optimal parameter combination (K1L1M2) was identified through multi-response optimization, resulting in reduced yarn tension and a reduced yarn breakage rate, together with an improved cop diameter. Although single-response analyses yielded different optimum settings, the objective of second-stage optimization was to determine the parameter combination providing the best overall performance across all responses simultaneously. While top-ring rail yarn tension and cop diameter was optimized at K1L1M1, bottom-ring rail tension, cop diameter, and the yarn breakage rate consistently favored M2 (111 mm). Consequently, K1L1M2 achieved the highest composite score and was selected as the global optimum because it provided the most balanced combination of low yarn tension, favorable cop geometry, and a reduced yarn breakage rate. Thus, the selected optimum represents the best compromise among all investigated responses rather than the optimum condition for any individual response.

Regression analysis showed that traveler mass, spindle speed, and doff stage influenced process responses. Yarn tension was primarily affected by traveler mass; this is consistent with the regression coefficients, where K_1 had the largest negative effect and K_3 had the largest positive effect for both tb and tt, indicating lower tension at lower traveler mass levels and higher tension at higher levels, respectively. Similarly, spindle speed influenced yarn tension, with L_1 associated with reduced tension and L_3 with increased tension, as reflected by the negative and positive coefficients, respectively. The effect of doff stage differed between positions, with M_2 associated with reduced tension at the bottom ring

rail (tb), while M_1 showed the strongest negative effect for the top ring rail (tt), indicating positional differences in parameter influence.

Cop diameter was predominantly governed by the doff stage (M), which made the largest contribution in the regression models for cb and ct. The intermediate doff stage (M2) was associated with increased cop diameter at the bottom ring rail, whereas the top cop diameter was maximized at M1, indicating that the optimal doff stage differs between the bottom and top ring rail positions. This is consistent with the regression coefficients, as M2 had a strong positive effect on cb, while M1 had the largest positive coefficient for ct. This behavior may be associated with the influence of doff stage on the vertical position of the ring rail, with lower positions corresponding to higher cop diameter values compared to higher positions.

The regression model for the yarn breakage rate identified spindle speed and doff stage as the most influential parameters. Minimum breakage was associated with L_1 and M_2, while traveler mass showed a weaker effect. These parameters have been previously identified as critical for spinning stability [54], while, in this study, their combined and position-dependent effects were further clarified. The selection of M2 as the global optimum reflected the compromise inherent in multi-response optimization, balancing tension control, cop formation, and breakage across the full winding cycle.

4. Conclusions

In this study, the effects of critical ring spinning parameters—traveler mass (K), spindle speed (L), and doff stage (M)—on yarn tension, cop diameter, and end breakage were systematically evaluated using a Taguchi L9 orthogonal array and a normalization-based composite scoring framework. The results showed that traveler mass was the dominant factor influencing yarn tension, contributing 65.48% and 73.29% of the total variance at the bottom and top ring rail positions, respectively, with the lowest traveler mass (K1: 60 mg) yielding the lowest tension levels. The doff stage was identified as the primary factor governing cop diameter, particularly at the bottom rail, contributing 89.43% of the total variance, with the intermediate level (M2: 111 mm) producing the highest mean diameter and the most favorable S/N ratio. The yarn breakage rate was mainly influenced by doff stage (57.26% of the total variance) and spindle speed (41.89%), with optimal conditions observed at M2 (111 mm) and L1 (12,900 min^{-1}). The composite scoring approach identified K1L1M2 as the optimal parameter combination, achieving reduced yarn tension and breakage with improved cop diameter. The regression models demonstrated a high goodness-of-fit ($R^2 > 0.991$) within the experimental design space. The proposed framework provides a scalable tool for multi-objective optimization in ring spinning and supports the transition toward data-driven manufacturing systems. This study was conducted using a single yarn count (20 tex), a cotton–polyester blend composition (51/49), and a specific ring-spinning machine configuration. Therefore, the reported factor contributions and optimum parameter combination should be interpreted within the investigated experimental domain. Furthermore, the Taguchi L9 orthogonal array primarily evaluates main effects, so potential interactions among traveler mass, spindle speed, and doff stage were not explicitly quantified. Despite these limitations, the proposed methodology provides a robust and transferable framework for systematic multi-response optimization in ring spinning. In future studies, scholars should validate the findings across different yarn counts, fiber blends, and machine configurations while investigating interaction effects using more comprehensive experimental designs.

Supplementary Materials: The following supporting information can be downloaded at: https://doi.org/10.5281/zenodo.19857933. Python code for phase I and II: Taguchi analysis (Phase I) and composite scoring optimization (Phase II).

Author Contributions: Conceptualization, E.T. and S.P.; methodology, E.T.; software, S.P.; validation, E.T. and S.P.; formal analysis, E.T. and S.P.; investigation, E.T.; resources, E.T.; data curation, E.T. and S.P.; writing—original draft preparation, E.T. and S.P.; writing—review and editing, E.T.; visualization, E.T.; supervision, E.T. All authors have read and agreed to the published version of the manuscript.

Funding: This research received no external funding.

Data Availability Statement: The original contributions presented in this study are included in the article/Supplementary Materials. Further inquiries can be directed to the corresponding author.

Conflicts of Interest: The authors declare no conflicts of interest.

References

1. Toshikj, E.; Mladenovikj, N. Smartphone-based digital image processing for fabric drape assessment. *Textiles* **2025**, *5*, 63. [CrossRef]
2. Bermeo-Giraldo, C.M.; Valencia-Arias, A.; Rojas, M.E.; Carona-Acevedo, S.; Rodrigues-Correa, A.P.; Gonzalez-Ruiz, D.J.; Londono-Celis, W.; Carcia, B.R. Research agenda on the evolution of digital transformation in the textile sector: A bibliometric analysis and research trends. *Discov. Sustain.* **2025**, *6*, 294. [CrossRef]
3. Toshikj, E.; Petrovski, O.; Petrovska, M.; Jordanov, I. Antimicrobial chitosan-based cotton yarns: Effect of chitosan solution concentration. *Tekstilec* **2023**, *66*, 116–125.
4. Toshikj, E.; Jordanov, I.; Dimova, V.; Mangovska, B. Influence of various pre-treatment processes on selective oxidation of cotton yarns. *AATCC J. Res.* **2023**, *4*, 22–28.
5. Toshikj, E.; Jordanov, I.; Dimova, V.; Mangovska, B. The influence of non-selective oxidation on differently pre-treated cotton yarns properties. *Mater. Sci.* **2016**, *22*, 429–434. [CrossRef]
6. Čubrić, S.I.; Čubrić, G. Influence of yarn and fabric properties on mechanical behavior of polymer materials and its retention over time. *Polymers* **2024**, *16*, 1725. [CrossRef]
7. Toshikj, E.; Demboski, G.; Jordanov, I.; Mangovska, B. Functional properties and seam puckering on cotton shirt influenced by laundering. *Tekstilec* **2019**, *62*, 4–11. [CrossRef]
8. Toshikj, E.; Jordanov, I.; Demboski, G.; Mangovska, B. Influence of multiple laundering on cotton shirts properties. *Tekst. Konfeksiyon* **2016**, *26*, 393–399.
9. Toshikj, E.; Demboski, G.; Jordanov, I.; Mangovska, B. Influence of seam type and laundering on seam puckering and functional properties of cotton/polyester shirt fabrics. *AATCC Rev.* **2015**, *15*, 41–49. [CrossRef]
10. Abdkader, A.; Hossain, M. A critical review on recent developments and solutions in high-speed ring spinning process. *Tex. Res. J.* **2023**, *93*, 5485–5504. [CrossRef]
11. Ahmed, N.; Hossen, J.; Ali, S.M. Improvement of overall equipment efficiency of ring frame through total productive maintenance: A textile case. *Int. J. Adv. Manuf. Technol.* **2022**, *94*, 239–256.
12. Hossain, M.; Abdkader, A.; Nocke, A.; Unger, R.; Krzywinski, F.; Hasan, M.M.B.; Cherif, C. Measurement methods of dynamic yarn tension in a ring spinning process. *Fibres Text. East. Eur.* **2016**, *24*, 36–43. [CrossRef]
13. Islam, D.M.; Rokonuzzaman, M.; Saha, J.; Razzaque, A. Effect of machine setting parameters on ring slub carded yarn quality and spinning procedure. *J. Tex. Sci. Technol.* **2017**, *3*, 45–55.
14. Kanon, A.T.; Rashid, E.; Islam, A. An analogical method for evaluating ring performance based on quality and production parameters. *Heliyon* **2023**, *9*, e19424. [CrossRef] [PubMed]
15. Dey, K.P.; Das, B.; Islam, S.; Das, P.K.; Chowdhury, A. Determination of suitable traveler for definite yarn count: A comparative study. *Glob. J. Eng. Technol. Adv.* **2021**, *9*, 036–049. [CrossRef]
16. Miah, L.; Sharmin, N.; Yasmin, J. Impact of spindle speed and traveler weight in the tensile properties of yarn explicitly the yarn tenacity and elongation at break. *Int. J. Innov. Sci. Eng. Technol.* **2019**, *6*, 2348–7968.
17. Li, X.; Liu, H.; Lv, P.; Liu, L. Theoretical model for the motion of a ring spinning traveler. *J. Text. Inst.* **2020**, *112*, 406–416. [CrossRef]
18. Hossain, M.; Sparing, M.; Espenhahn, T.; Abdkader, A.; Cherif, C.; Huhne, R.; Nielsch, K. In situ measurement of the dynamic yarn path in a turbo ring spinning process based on the superconducting magnetic bearing twisting system. *Text. Res. J.* **2020**, *90*, 951–968.
19. Tang, B.H.; Xu, G.B.; Tao, M.X.; Feng, J. Mathematical modeling and numerical simulation of yarn behavior in a modified ring spinning systems. *Appl. Meth. Model.* **2011**, *35*, 139–151. [CrossRef]

20. Hossain, M.; Telke, C.; Abdkader, A.; Sparing, M.; Espenhahn, T.; Huhne, R.; Cherif, M.; Beitelschmidt, M. Mathematical modelling of dynamic yarn path considering the balloon control ring and yarn elasticity in the ring spinning process based on the superconducting bearing twisting element. *Text. Res. J.* **2018**, *26*, 32–40. [CrossRef]
21. Rezahasani, M.; Savadroobdari, H.A.; Razbin, M.; Johari, M.S. Optimizing drawing frame variables to enhance polyester spun yarn quality using soft computing techniques. *Sci. Rep.* **2025**, *15*, 18815. [CrossRef] [PubMed]
22. Shahzad, S.A.; Ahmad, Z.; Ali, Z.; Afzal, A.; Qadir, B.M.; Khaliq, Q.M. Statistical analysis of yarn to metal friction coefficient of cotton spun yarn using Taguchi design of experiment. *J. Strain Anal. Eng. Des.* **2018**, *53*, 485–493. [CrossRef]
23. Ghorbani, K.; Hasani, M.; Zarrabini, M.; Saghafi, R. An investigation into sound transmission loss by polypropylene needle-punched nonwovens. *Alex. Eng. J.* **2016**, *55*, 907–914. [CrossRef]
24. Chakraborty, S.; Mitra, A. A multivariate quality loss function approach for optimization of spinning. *J. Inst. Eng. India Ser. E* **2018**, *99*, 101–109. [CrossRef]
25. Haq, N.U.; Khan, R.M.; Khan, M.A.; Hasanuzzaman, M.; Hossain, R.M. Global initiatives for industry 4.0 implementation and progress within the textile and apparel manufacturing sector: A comprehensive review. *Int. J. Comput. Integr. Manuf.* **2025**, *38*, 1637–1662. [CrossRef]
26. Liang, J.; Huang, J.; Wu, G.; Wu, W. Multi-output linear regression-based yarn and fabric spectra prediction. *Color Res. Appl.* **2025**, *51*, e70013.
27. Nouinou, H.; Asadollahi-Yazdi, E.; Baret, I.; Nguyen, Q.N.; Terzi, M.; Ouazene, Y.; Yalaoui, F.; Russell, K. Decision-making in the context of industry 4.0: Evidence from the textile and clothing industry. *J. Clean. Prod.* **2023**, *391*, 136184. [CrossRef]
28. Oncul, K. Quality optimization and process capability analysis of ring spun Suprima cotton yarn. *Mater. Test.* **2021**, *63*, 943–949.
29. Hossen, J.; Saha, K.S. Influence of blending method and blending ratio on ring-spun yarn quality—A MANOVA approach. *Tekstilec* **2023**, *66*, 227–239.
30. Wolf, H.; Rieche, A. Simulation and experimental validation of a ring spinning process. *Simul. Model. Pract. Theory* **1999**, *14*, 809–816.
31. Tang, X.Z.; Fraser Barrie, W.; Wang, X. Modelling yarn balloon motion in ring spinning. *Appl. Math. Model.* **2007**, *31*, 1397–1410. [CrossRef]
32. Wu, X.; Hurren, C.; Li, W.; Wang, X. Numerical analysis of heat transfer in ring spinning. *Text. Res. J.* **2022**, *92*, 3990–4007. [CrossRef]
33. Prendžova, M. The effect of cotton yarn properties on yarn end breakage. *Int. J. Polym. Mater. Polym. Biomater.* **2000**, *47*, 701–707. [CrossRef]
34. Maheswaran, R.; Srinivasan, V. Model-cotton fibre blend ratio and ring frame parameters optimization through the Taguchi method. *AUTEX Res. J.* **2019**, *19*, 86–96. [CrossRef]
35. Kalayci, E.; Avici, O. The disperse dying of polyethermide fibers using orthogonal array (Taguchi) design. *Fibers Polym.* **2024**, *25*, 3045–3060.
36. Wang, C.; Chen, Q.; Hussain, M.; Wu, S.; Chen, J.; Tang, Z. Application of principal component analysis to classify textile fiber based on UV-Vis reflectance spectroscopy. *J. Appl. Spectrosc.* **2017**, *84*, 391–395.
37. Kumar, P.; Almeida, F.; Ar, A.; Al-Mdallal, Q. Construction of optimized theoretical model using ANOVA-Taguchi methodology for transient flow of Carreau nanofluid through microchannel prone to radiation. *Alex. Eng. J.* **2025**, *112*, 411–423.
38. Younes, B.; Fotheringham, A. Factorial optimization of the effects of melt-spinning conditions on biodegradable as-spun aliphatic-aromatic copolymer fibers. III. Diameter, tensile properties, and thermal shrinkage. *J. Appl. Polym. Sci.* **2011**, *122*, 1434–1449. [CrossRef]
39. Yu, H.; Xu, G.; Yang, S.; Jiang, W.; Jiang, L.; Xu, W. A method to regulate the shape of yarn balloon and its effect on the tension and quality of ring spun yarn. *Fibers Polym.* **2024**, *25*, 1149–1162. [CrossRef]
40. Hasanuzzaman, D.P.K.; Basu, S. Optimization of ring-spinning process parameters using response surface methodology. *J. Text. Inst.* **2014**, *106*, 510–522. [CrossRef]
41. Chen, L.X.; Mei, Q.S.; Chen, B.X. Non-contact measurement of yarn tension in spinning process. *Appl. Mech. Mater.* **2014**, *722*, 367–372. [CrossRef]
42. Yu, H.; Zhang, J.; He, S.; Feng, P.; Yang, C. Mathematical model of multisegment balloons in ring spinning. *Text. Res. J.* **2023**, *93*, 3069–3080. [CrossRef]
43. Praček, S. The effects of the tension on the yarn dynamics. *J. Text. Inst.* **2024**, *116*, 594–602. [CrossRef]
44. Zhen, C.; Shunqi, M.; Zhiming, Z. Yarn tension measurement of ring spinning balloon based on MATLAB image processing technology. *Comput. Sci. Math.* **2024**, *9*, 325–336. [CrossRef]
45. Praček, S.; Halasz, M. Modelling of tension in yarn package unwinding. *Ind. Text.* **2021**, *72*, 256–260. [CrossRef]
46. Joha, Y.M.; Morad, E. Study the specifications of the thread through the construction of the pipe on the ring spinning machine. *J. Biomed. Sci. Eng.* **2015**, *8*, 295–319.

47. Cui, P.; Zhang, Y.; Xue, Y. Detection and analysis of real-time dynamics of yarn tensions in a ring spinning frame. *J. Fiber Sci. Technol.* **2020**, *76*, 190–198. [CrossRef]
48. Ciu, P.; Zhang, Y.; Xue, Y. A novel method of analyzing spinning tensions for yarn breakage detection in ring frame. *J. Eng. Fibers Fabr.* **2020**, *15*, 1–12. [CrossRef]
49. Perez-Delgado, J.Y.; Beitelschmidt, M.; Hossain, M.; Cherif, C.; Abdkader, A.; Baloochi, M.; Huhne, R. Control ring and air drag effects on yarn balloon dynamics in ring spinning: A spring-mass modeling approach. *Multibody Syst. Dyn.* **2025**. [CrossRef]
50. Hossain, M.; Telke, C.; Abdkader, A.; Cherif, C.; Beitelschmidt, M. Mathematical modelling of the dynamic yarn path depending on spindle speed in ring spinning process based on superconducting magnetic bearing. *Text. Res. J.* **2015**, *86*, 10180–11190.
51. Murugesan, M.; Senthikumar, T.; Nayar, C.R. A study of collapsed balloon spinning and its effect on cotton yarn properties. *J. Polym. Text. Eng.* **2015**, *2*, 44–49.
52. Ali, M.; Ahmed, R.; Amer, M. Yarn tension control techniques for improving polyester soft winding process. *Sci. Rep.* **2021**, *11*, 1060. [CrossRef] [PubMed]
53. Quan, J.; Chen, L.; Yu, J.; Xue, W. Numerical analysis and experimental investigation of a multi-principle drafting in ring spinning. *Text. Res. J.* **2022**, *92*, 1940–1951.
54. Alam, P.F.B.; Islam, M.T.; Hossan, M.M. Assessing the impact of speed change on energy consumption and productivity: Investigating ring frame process parameters. *Text. Leather Rev.* **2022**, *5*, 509–524. [CrossRef]